Chapter 3

Synthesis and Characterization Techniques

3.1 Overview

The experimental work's backbone is understanding the instruments and the principles behind their functioning. The present thesis deals with an experimental study of the synthesis and magnetic resonance characterization of the YIG and TmIG thin films. Therefore, giving a perspective on the experimental instruments is essential. Understanding the instrument gives an additional advantage regarding the outcomes and their analysis. This appeals to the current chapter to present a brief introduction to the method of synthesis and characterization techniques. The thesis compares the cost-effective deposition method, i.e., sol-gel-based spin-coating, with previous sophisticated methods. This chapter gives a comprehensive synthesis detail along with an overview of XRD, XRR, SEM, AFM, XPS, SQUID-VSM, and FMR.

3.2 Synthesis method

The method of deposition used in this thesis is sol-gel-based spin coating. Iron garnets thin films can be prepared using LPE [87], PLD [88, 89, 90] and rf-sputtering [91, 92, 93]. All the above processes require sophisticated instruments and are expensive methods. One alternative to these methods is all wet chemical-based methods; sol-gel-based spin coating is one of them. To deposit the samples using sol-gel-based spin-coating, cleaning the substrate and preparing the solution of appropriate molarity is essential to get enough grain density on the substrate along with the rotation speed of the spin-coater and duration and stages of annealing. All these factors are comprehensively discussed in the subsections. The primary reaction for the chemical synthesis is given below:

$$3X(NO_3)_3 + 5Fe(NO_3)_3 = X_3Fe_5O_{12} + 12N_2O_5 \tag{3.1}$$

Where X is yttrium (Y) or thulium (Tm). This thesis used nitrates of iron, yttrium, and thulium as the precursors. Nitrates dissolve in the 2-methoxyethanol and dissociate into the metal and nitrate ions; these metal ions hydrolyze at the specific pH and oxidize to give the final oxide phase as per the stoichiometry after the annealing [94].

3.2.1 Substrate Cleaning

Cleaning the substrate from dust and organic and inorganic residue is essential to grow the thin film onto the substrate. For this thesis, 1×1 cm^2 dimensions of single crystal thermally oxidized Silicon substrate (SiO_2/Si <100>) and gadolinium gallium garnet (GGG) <111> oriented substrates have been used. A pen diamond cutter was used to cut the SiO_2/Si substrate, and manufacturers cut GGG substrates. Firstly, to remove the dust and any residue on the substrate, it was cleaned with soap water with cotton buds by rubbing soapy buds in a circular motion, then rinsing the substrate with deionized water (DI), followed by

ultrasonication of it for 30 minutes in DI water, then 30 minutes ultrasonication in Acetone and Isopropyl alcohol, respectively, and remove any dust and other unwanted species of the substrate surface. At the end of substrate surface activation and organic residue burning were achieved by plasma-cleaned at atmospheric pressure.

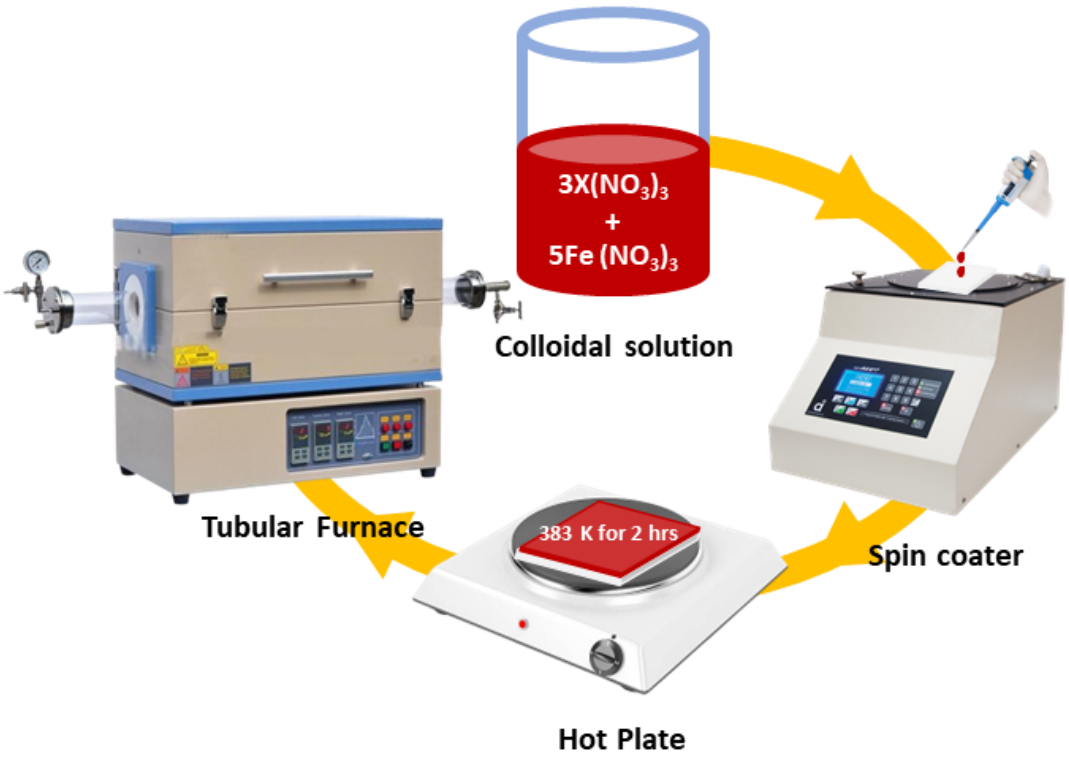

Fig. 3.1 *Schematic of spin coating deposition.*

3.2.2 Solution Preparation

For the solution of precursors, $Y(NO_3)_3.6H_2O$ or $Tm(NO_3)_3.6H_2O$ and $Fe(NO_3)_3.9H_2O$ were dissolved in 2-methoxyethanol in 3:5 ratio forming 400 mM solution. pH is maintained to 2-3 using diethylamine. This precursor solution was stirred on a magnetic stirrer at room temperature for three days. Before the deposition day, the solution was filtered using a syringe filter of 0.47 μm pore size to get a homogeneous colloidal solution and remove the bigger chunks formed while balancing the pH using the diethylamine.

3.2.3 Spin Coating and Annealing Procedure

Figure (3.1) shows the schematic of the deposition procedure. The filtered solution was drop cast over a cleaned substrate and spin-coated at 4000 rpm for 30 s. To evaporate the solvent from the coated substrate, it is heated at 363 K for 2 hrs, followed by green heating at 623 K for 30 min for the organic compound dissociation. The final product is annealed at 1173 K for 5 hrs (YIG) and 1223 K for 3 hrs (TmIG) to get a single-phase iron garnet.

3.3 Characterization Techniques and their principles

3.3.1 X-ray Diffraction

X-rays were discovered by German physicist R*ö*ntgen in 1895 [95]. X-rays propagate in a straight line and can diffract and interfere. X-rays have various applications in the medical, chemistry, and physics fields. Its first application was in radiography by physicians to observe broken bones [96]. Later, they began to see through the opaque things due to the penetration capability of X-rays through lighter elements. In 1912, XRD through the crystals was observed and utilized after discovering the essential nature of X-rays [97]. As X-rays have a wavelength of a few Å, which is the order of the interplanar distances in the crystals, this property of X-rays makes them a handy tool for resolving the crystal structure of the materials. Materials scientists, along with chemists, physicists, and various engineers utilized this characterization method to confirm the crystalline state of the solids. M. Von Laue discovered the XRD in 1912 and was awarded the Nobel Prize in Physics 1914 [98, 99], and W.H. Bragg and W. L. Bragg did a more straightforward explanation of the XRD in 1913 and awarded the Nobel Prize in Physics 1915 [100, 101].

Working Principle and Instrumentation

Laue explained XRD using scattering of the X-ray from the atoms. The simpler equation was presented by Bragg and Bragg, considering the atoms arrange themselves in the periodic planar manner, and interplanar distance gives the diffraction at various angles based on their Miller indices (hkl) and wavelength of the incident X-ray. The uncomplicated equation originated by them is as follows [97]:

$$2dsin\theta = n\lambda \tag{3.2}$$

Figure (3.2) is the schematic of Bragg's assumption, taking that each layer of the atoms in the unit cell as a plane and the diffraction of the incident X-ray wavelength of these planes. The wavelength of the incident X-ray is λ, and the interplanar distance is d. Assuming constructive interference, the path difference between the X-rays traveling between two successive layers equals $n\lambda$, as in equation (3.2) [56].

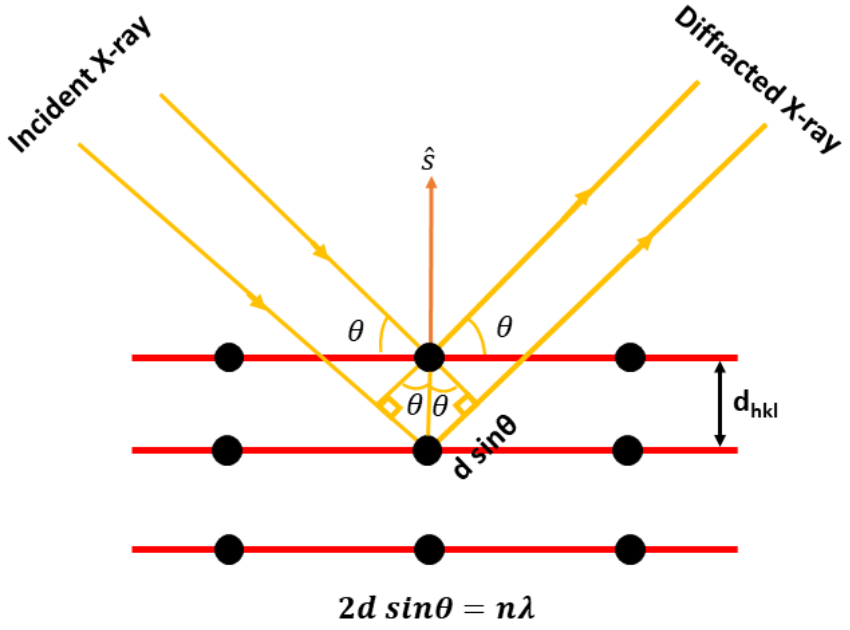

Fig. 3.2 *Schematic of Bragg's diffraction.*

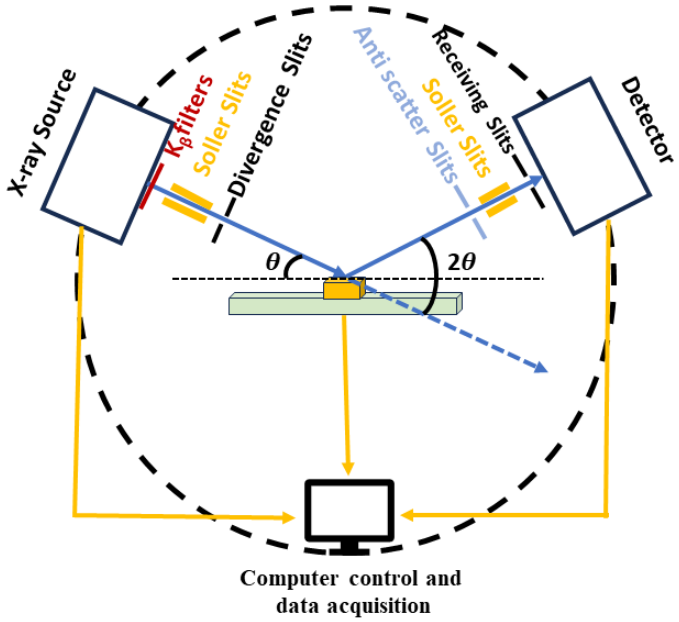

Fig. 3.3 *Schematic of the instrument of the XRD* .

Figure (3.3) depicts the XRD instrumentation, comprising of the X-ray source, sample goniometer, and detector. The X-ray source is fabricated of anode and cathode sealed in a vacuum tube. AC current is passed through the anode (tungsten filament), which emits an electron that collides with the cathode (copper anode connected with the water cooling system). These colliding electrons knock out core electrons in the Cu cathode and further de-excite higher orbital electrons by emission of the X-rays. These X-ray comprise Bremsstrahlung and the characteristic emission peaks [102]. In Cu K characteristic spectra, Cu K_α and Cu K_β are present. The Ni filter has been used to eradicate the Cu K_β, which is the low-intensity peak. Ni has the K absorption edge at 8333 eV, and the energy value of the Cu $K_{\alpha 1}$, Cu $K_{\alpha 1}$ and Cu K_β are 8048 eV, 8027 eV, and 8905 eV, respectively [103, 104]. The energy range of the Cu K_β lies above the Ni K absorption edge; it eradicates the Cu K_β from the X-rays source spectrum. In this thesis, Cu K_α has been utilized, with wavelength 1.5406 Å. Cu $K\alpha_1$ and $K\alpha_2$ are present due to the low wavelength separation

between the two and the average final wavelength taken of the two wavelengths. Both $\theta/2\theta$, and $\omega - 2\theta$ measurements has been done in Bragg-Brentano geometry.

This thesis discusses the XRD of both polycrystalline and epitaxial thin films. In epitaxial films, only a single family of the crystallographic planes are present as the other plane normal [hkl] is not parallel to the diffraction vector ($\hat{S}$). Bruker D8 and Panalytical X'Pert Pro diffractometers with Cu-K_α (λ = 1.5406 Å) as a radiation source are used in the present thesis for the polycrystalline samples [105, 106]. For the epitaxial thin films grazing-incident XRD has been done at INDUS2 (BL13), of the RRCAT, Indore [107] at 10 KeV energy of the wavelength 1.24 Å. The Joint Committee on Powder Diffraction Standards (JCPDS) files are used to confirm the experimental XRD patterns. As the crystal structure is cubic, interplanar distances are are calculated using Bragg's relation 3.2. The d spacing is used to calculate lattice parameter (a) using:

$$d = \frac{a}{\sqrt{h^2 + k^2 + l^2}} \tag{3.3}$$

3.3.2 X-ray Reflectivity

X-rays are the non-destructive tool to study the thin film properties of the films. XRR has been based on the small angle interactions of the X-rays and the different interfaces and electron density layers present in the thin films. Each layer has a different electron density, and the relative electron density of the layer decides the critical angle of the reflection of the incident X-rays in the spectra. Above the critical angle of reflection, X-rays penetrate the thin film and reflect from the different interfaces, depending on the thickness and the roughness of the layers and the interface, and interfere. This interference gives reflectivity spectra that include the Kiessig fringes. The periodicity of the Kiessig fringes depends on the thickness of the layers. Surface and interface roughness contributes to the spectra'

slope with the increased incident angle. As the roughness increases, more X-ray gets scattered diffusely, and specular reflectivity reduces, which reduces the slope more rapidly. Bruker D8 was used to perform XRR on the thin films. XRR can differentiate thicknesses from 3 - 120 nm [108]. Roughness can be analyzed in the range of 0 - 2 nm.

Working Principle and Instrumentation

Parratt's formalism and Fresnel's reflection principle are used to understand the total external reflection of X-rays in thin films. Before deriving the equation for the Parratt formalism, here are basic terms, i.e., scattering vector (q_z) and the critical angle (θ_C). The scattering vector is the difference between the final and initial wave vector, k_f and k_i, respectively. The only non-vanishing term in specular reflectivity is the out-of-plane wave vector (k_z); for the incident wavelength λ, $q_z = \frac{4\pi}{\lambda} \sin\theta$. Further, the critical angle (θ_C) is the angle of total eternal reflection. The scattering factor for θ_C is $q_C = \frac{4\pi}{\lambda} \sin\theta_C$ and at small angles $q_C = \frac{4\pi}{\lambda}\theta_C$ after the rearrangement $\theta_C = q_C\frac{\lambda}{4\pi}$. Figure (3.4) represents schematics of the XRR spectra showing critical angle and the Kiessig fringes in it.

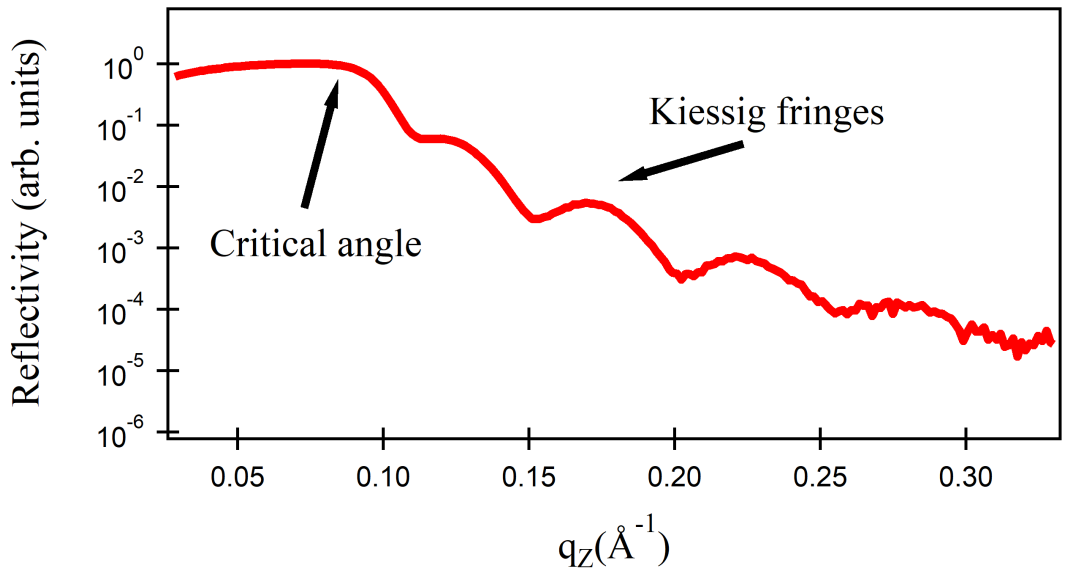

Fig. 3.4 *A schematic XRR showing critical angle and the Kiessig fringe.*

The Fresnel equation was used for the single interface system to resolve the X-ray reflectivity [109]. In which reflectivity as a function of scattering vector according to the Fresnel equation is:

$$R(q) = \left| \frac{q_z - \sqrt{q_z^2 - q_C^2 - \frac{32i\pi^2\beta}{\lambda^2}}}{q_z + \sqrt{q_z^2 - q_C^2 - \frac{32i\pi^2\beta}{\lambda^2}}} \right|^2 \tag{3.4}$$

At various q values, reflectivity vary differently, and the different conditions are as follows:

1) if q_z<q_C, total external reflection occurs, and R=1.

2) if q_z=q_C, Reflection reduces extensively.

3) if q_z>q_C, R decreases with $\frac{1}{q^4}$ as R= $\frac{q_C^4}{16q^4}$

Based upon the Fresnel reflection, multilayer XRR analysis is performed using Parratt's formalism [110]. This thesis used Parratt32 software to perform the fittings based on Parratt's formalism. It uses the least square fitting for the parameter minimization.

3.3.3 Atomic Force Microscopy

A three-dimensional microscopy performed by contacting a nano-probe and sample surface is called AFM. Surface morphology studies of the non-conductive samples allow for assessing surface texture and roughness. AFM can be performed in contact, tapping, and non-contact mode. The separation between the probe and sample causes the bending of the cantilever in different orientations. Figure (3.5) shows the different modes with probe-sample separation.

Working Principle and Instrumentation

The AFM setup comprises a laser and probe attached to the cantilever, which has been adjusted by the piezoelectric scanner, sample stage, and photodiode detector. Figure (3.6)

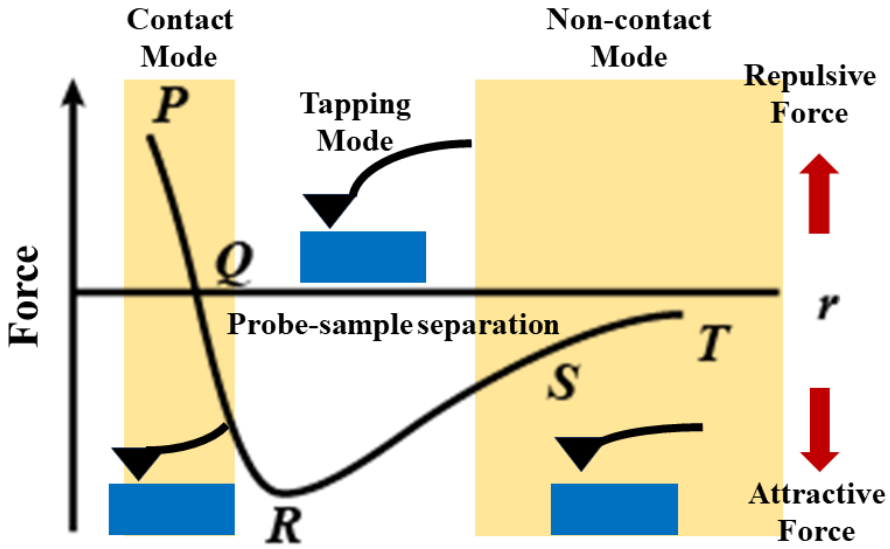

Fig. 3.5 *Different mode of AFM to separation between probe and sample.*

depicts the instrumentation of the AFM. The sample is exposed to the probe tip connected to the piezoelectric scanner to tune the distance between the probe and the sample. The laser is focused on the top of the tip and, dependent on its position, reflects the laser to the photodiode. If the laser is at the center, it is at zero feedback. If it gets deflected, it gives feedback to the piezoelectric scanner to move the probe, and that value is registered as data. This data forms the surface morphology micro-graph as a function of the scanning distance. This work studies the micro-graphs of the scan area 3×3 μm and 5×5 μm. The height sensitivity of the AFM used in this work is nm.

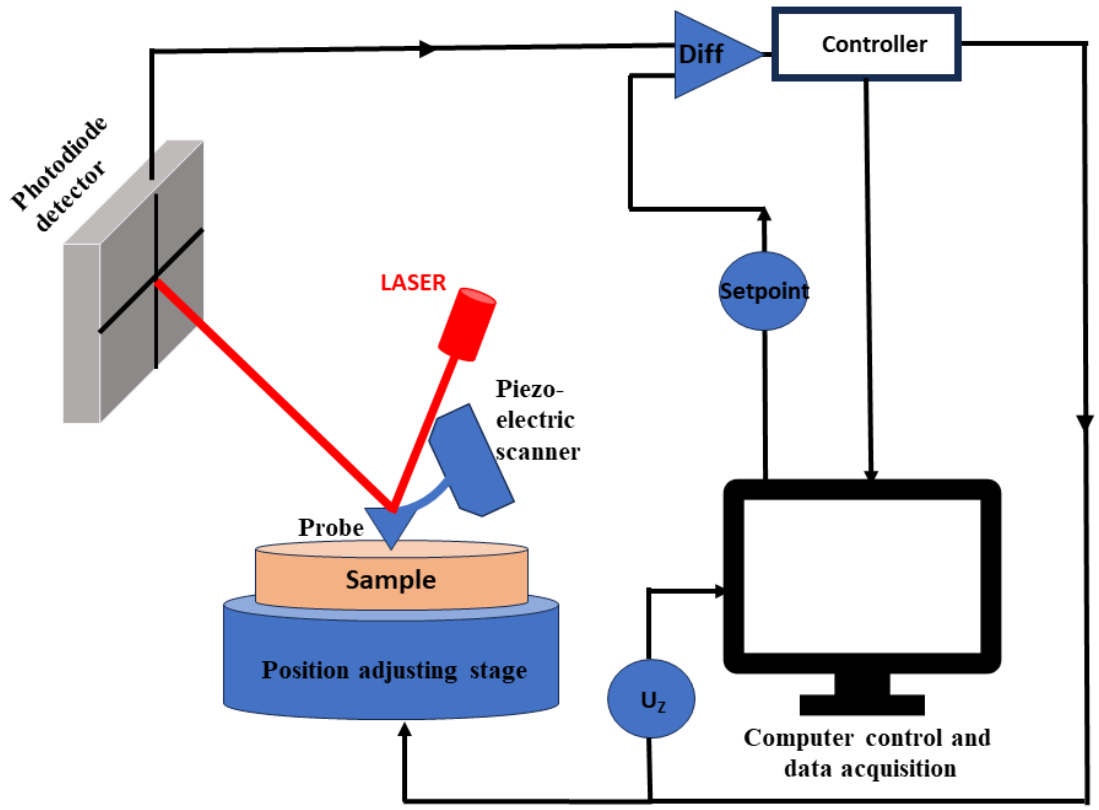

Fig. 3.6 *Schematics of the instrumentation of Atomic Force Microscopy.*

Bruker Anasys nano-IR3 in contact mode performs AFM in this thesis [111].

3.3.4 Scanning Electron Microscopy

The electron beam generation and the interaction with the matter are interesting phenomena that have resulted in the development of various characterization techniques, namely, SEM, transmission electron microscopy, and scanning transmission electron microscopy. Here, this section gives a brief description of the working principle and the instrumentation of the SEM. This technique utilizes secondary emission electrons to provide information regarding the topography of the materials. With less than 50 eV energy, these low-energy electrons [112]. SEM can magnify the sample up to 200,000X. SEM uses a raster scanning process, which makes it a high-resolution, real-time scanning method.

Working Principle and Instrumentation

The incident primary electrons irradiate the sample surface, emitting elastic and inelastic electrons. Figure (3.7) depicts the energy distribution of emitted electrons from silver when it was irradiated with the primary electron of the 155 eV energy. The peak a represents the elastically reflected primary electrons. The small peak b represents the collodion having discrete energy losses. The broader peak c below the 50 eV energy represents the secondary electrons. These secondary electrons are the bound state electrons of the silver. The section between the b and c is backscattered, or the inelastically reflected primary electrons [113]. The broad peak of the secondary electrons illustrates their higher number density, and they are generated from the shallow region of the sample surface, making them suitable for the topographical information.

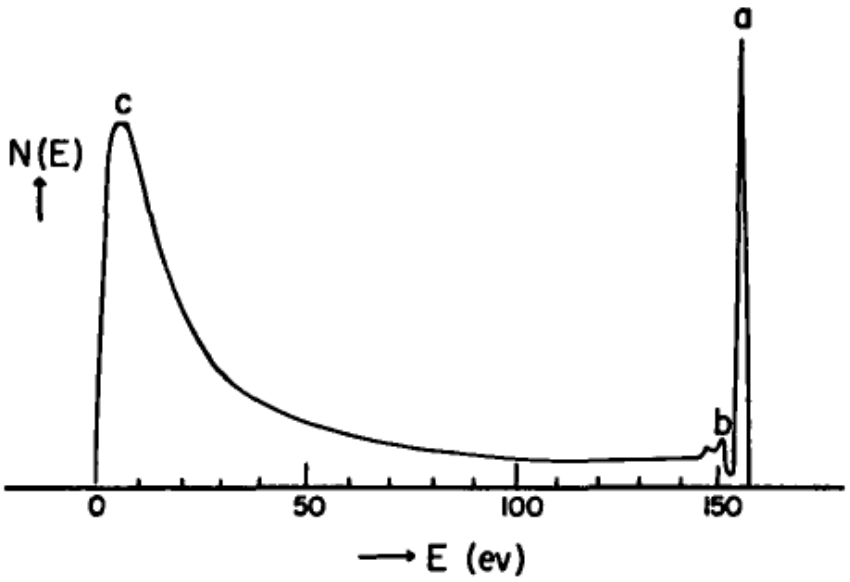

Fig. 3.7 *Energy distribution of electron emission, when Silver is bombarded with the primary electron of 155 eV energy, adapted by [113].*

SEM is a high vacuum microscopic instrument. Figure (3.8) depicts schematics of the components in SEM. The setup consists of an electron source, initially a tungsten filament. Nowadays, field-emitting guns (FEG) are used. FEG is also made of tungsten but in

the form of a tip (0.5 nm). They work at low temperatures, in the presence of anode, to eject out and accelerate the electrons. These electrons are accelerated using scan tilt and focused using condenser lenses. These electrons are passed through a scanner coil to focus the specific area. These electrons beam after irradiating the sample surface and interact with it [114]. Figure (3.9) depicts the interaction of the electron beam with the sample and, as a result, secondary electrons, backscattered electrons, Auger electrons, characteristic X-rays, Cathodoluminescence, and continuum X-rays emit. Out of these, secondary electrons can give the topographical information of the sample. Characteristic X-rays give the sample's elemental composition. Among these, secondary electrons are collected by the Everhart–Thornley detector [112].

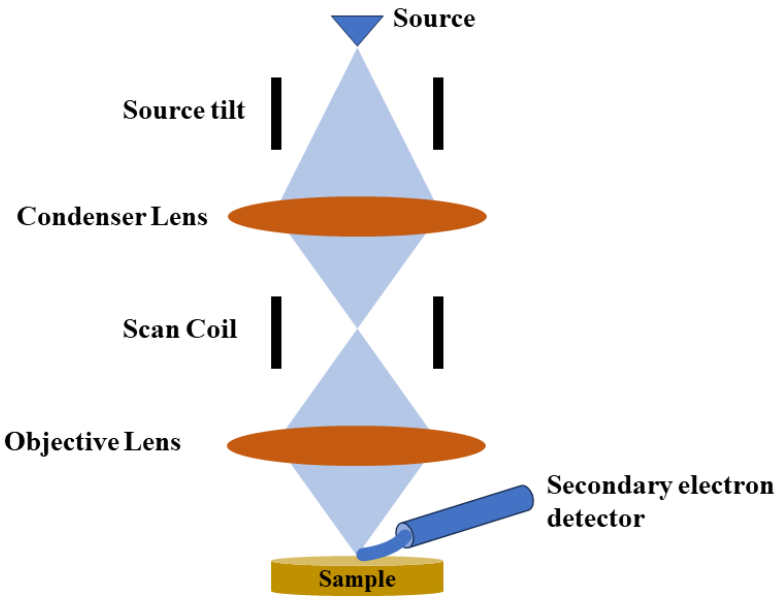

Fig. 3.8 *Instrumentation of Scanning Electron Microscope.*

This study studied insulating samples; therefore, a few nm thick gold coatings were used to overcome the screening effect of the accumulating electron. A field emission gun-based scanning electron microscope (FE-SEM) of SIGMA, ZEISS has been used in the presented thesis [115] at primary electron beam energy 15 keV. Image processing is performed using the ImageJ software [116].

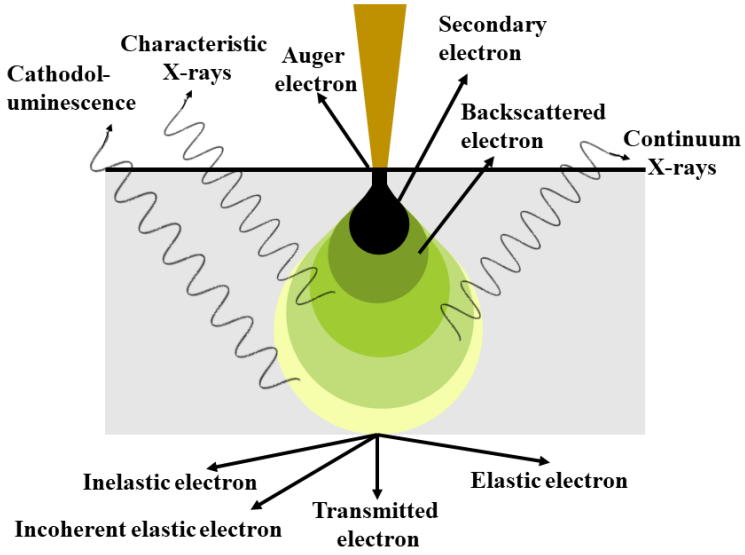

Fig. 3.9 *The interaction of focused electron beam eject out different kinds of electrons and X-rays.*

3.3.5 X-ray Photoelectron Spectroscopy

XPS is a sophisticated, ultra-high vacuum-based method to discover the information from the characteristic binding energy of the core electrons of the elements. XPS is surface-sensitive X-ray-based spectroscopy that determines the chemical composition with the valence state of the constituents. XPS is also known as electron spectroscopy for chemical analysis (ESCA) [117].

Working Principle and Instrumentation

XPS is based on the photoelectric effect. The photoelectric effect was discovered by Hertz in 1887, and Einstein utilized the concept of quantization of energy packets (quanta) to explain it in 1905, for which he was awarded the Nobel Prize in 1921 [118, 119]. Kai Seigbahn invented the XPS instrument in 1954 at Uppsala University, and for that, he was awarded the 1981 Nobel Prize in physics [120]. X-ray shined on the sample surface causes the ejection of the electron, and by measuring the energy of the ejected electron, the nature

of constituents and their environment is obtained, using the equation below,

$$E_B = E_P - (E_K + \phi) \tag{3.5}$$

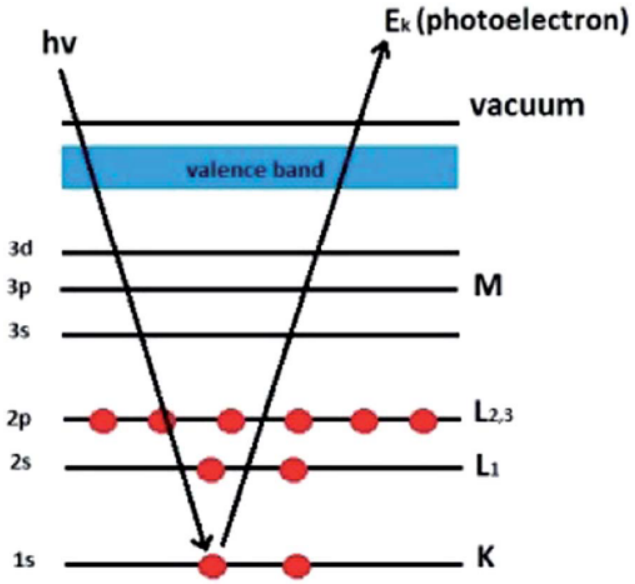

Fig. 3.10 *Schematic of photoelectric effect in XPS adapted by [121].*

where E_B is binding energy, E_P is incident photon energy, E_K is the kinetic energy of the ejected electron, and ϕ is the work function of the instrument and sample. When X-rays irradiate the material, its core electron gets ejected when the incident X-ray energy is higher than the material's work function, and the rest of the energy is converted into the E_K of the ejected electrons. If we take a difference of the incident energy, work function, and E_K, we get the E_B, a fingerprint of the element. Figure (3.10) depicts the schematic of the electronic configuration of the element.

Figure (3.11) depicts the schematics instrumentation of the XPS comprising an X-ray source, sample holder, analyzer, detector, signal processor, and readout. Here, aluminum is utilized as the cathode for X-ray waves. Quartz as monochromator separates the K_α,

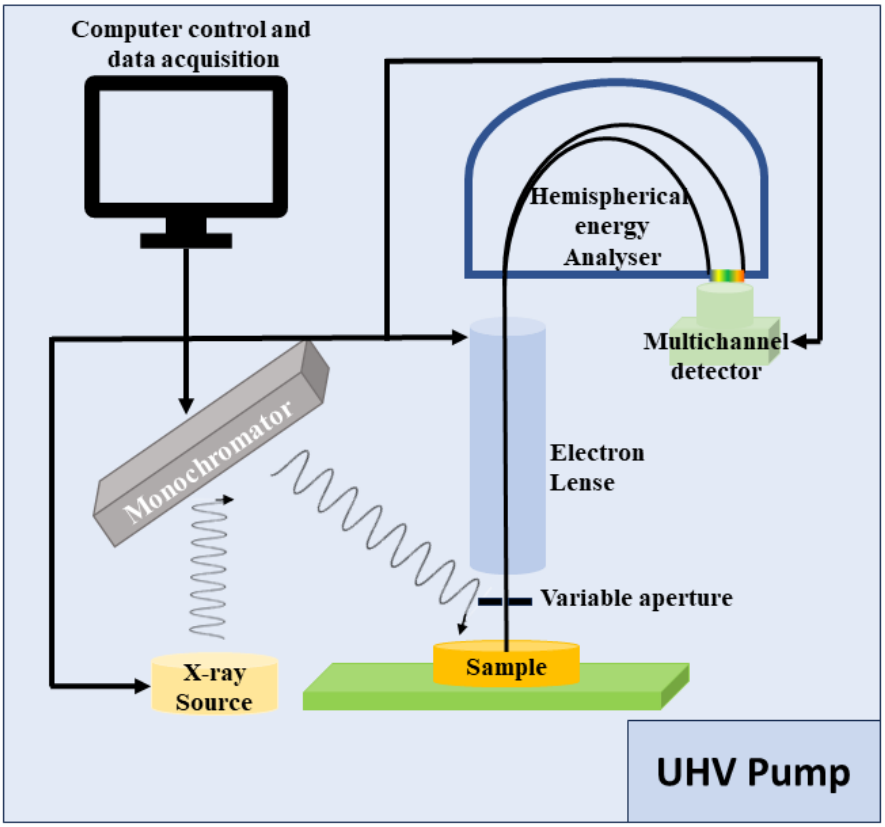

Fig. 3.11 *Schematic of instrumentation of XPS.*

centering at 1486.7 eV energy and bandwidth of 0.3 eV. This monochromatic light is incident on the sample surface. Photoelectrons are ejected, collected, and passed to the hemispherical analyzer to separate the electrons based on their kinetic energy. This count of that specific kinetic energy is converted into binding energy and is plotted as the spectra.

K-Alpha model of the Thermo Fisher Scientific is used to perform XPS in the present thesis [122]. This sample preparation chamber is vacuumed to $\approx 10^{-8}$ Torr, followed by the final chamber vacuum to $\approx 10^{-9}$ Torr. All core level XPS spectra were calibrated with respect to the C_{1s} peak centered at 284.8 eV.

3.3.6 Magnetic Property Measurement System

Magnetic Property Measurement System (MPMS) is the most sensitive magnetic moment measurement system that has sensitivity up to 10^{-8} emu [123]. It is versatile in measuring powder, thin films, single crystals, etc., and is widely used in materials science in studying hysteresis and magnetic phase transition using magnetization Vs temperature plots [50, 124]. MPMS combines vibrating sample magnetometry (VSM) and superconducting quantum interference device (SQUID). Where VSM gives rise to the flux change in the SQUID that measures the moment of the sample, the principle of VSM and SQUID will be discussed in the following section.

Working Principle and Instrumentation

VSM working Principle

VSM works on the principle of Faraday's law of electromagnetic induction. Current in a closed circuit is induced in the opposite direction when it is exposed to the varying magnetic flux [58]. This statement can be written as:

$$\varepsilon = -N\frac{\Delta\phi}{\Delta t} \tag{3.6}$$

Where ε is induced electromotive force, ϕ is flux.

SQUID working Principle

SQUID works on the principle of the Josephson tunneling effect. In 1962, Brian David Josephson theoretically predicted the tunneling of Cooper pairs across the insulating gap between two superconducting materials [125], which was later experimentally shown by Philip Anderson and John Rowell [126]. When an insulating or normal metal thin layer is sandwiched between two superconducting, Cooper pairs tunnels through that insulating or

regular conducting layers similar to electron tunnel through insulating layers in quantum tunneling. The current flow through the circuit will be [127]:

$$I = I_0 sin(\delta) \tag{3.7}$$

I_0 is the maximum current flow through the tunneling, and δ is the phase difference between the current of two superconducting layers [127].

$$\dot{\delta} = \frac{d\delta}{dt} = \frac{2eV}{\hbar} = \frac{2\pi}{\phi_0} V \tag{3.8}$$

where, ϕ_0 is flux quantization (h/2e) and V is volatge develope across the junction.

MPMS uses DC-SQUID, in which two parallel Josephson junctions sense the voltage induced by the change in flux. Figure (3.12) depicts the schematic diagram of DC-SQUID [127]. Figure (3.12) depicts the DC SQUID biased with current (I) and I bifurcate in two arms having value (I/2). Each Josephson junction causes a change in the phase difference of current passing through junctions and their interference with output current. The current induced (J) is due to applied flux causing phase difference in current flow and above I_C; voltage is induced as a function of applied change in magnetic flux. This induced voltage gives the moment of the samples.

Figure (3.13) depicts the IV characteristics of DC SQUID. Above I_C, Voltage starts to generate (I_0). IV characteristics at half-integer and integer flux quanta have different critical currents. Voltage is measured as a function of applied flux. Magnetometry measurements are conducted using Quantum design MPMS3 [123].

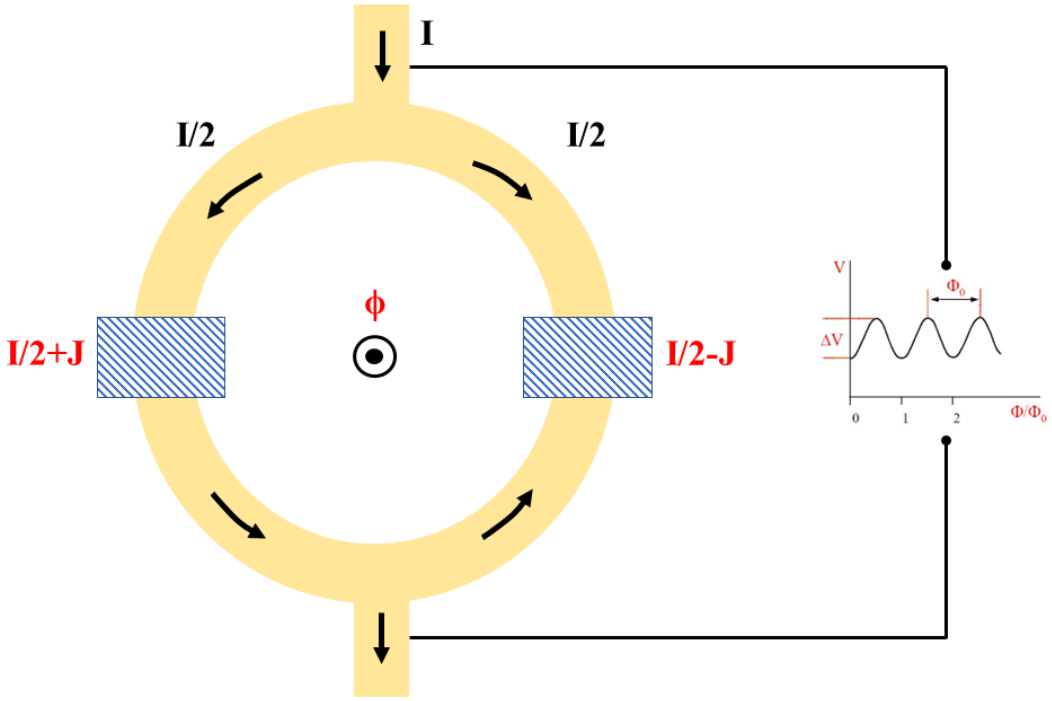

Fig. 3.12 *Schematic of Superconducting Quantum Interference device.*

DC Magnetometry

Magnetic materials have the transition from paramagnetic to ferromagnetic or antiferromagnetic phase as the function of the temperature. The magnetization of materials Vs temperature at a certain applied field gives the signature of this transition. Magnetization attains zero value at T_C, and a further temperature decrease enhances the moment until the mK temperature. At mK, it shows the highest magnetization by overcoming all thermal vibrations. This behavior is shown by ferromagnetic materials. Antiferromagnetic material's magnetization at T_N starts to decrease as the moments align in an anti-parallel manner. YIG and TmIG are antiferromagnetically coupled ferrimagnets. At a higher temperature, these materials show that ferrimagnetism gives the T_C at $\approx$ 560 K. In TmIG, on lowering the temperature, Tm^{3+} ion begins to contribute, and the moments decrease at T_N and

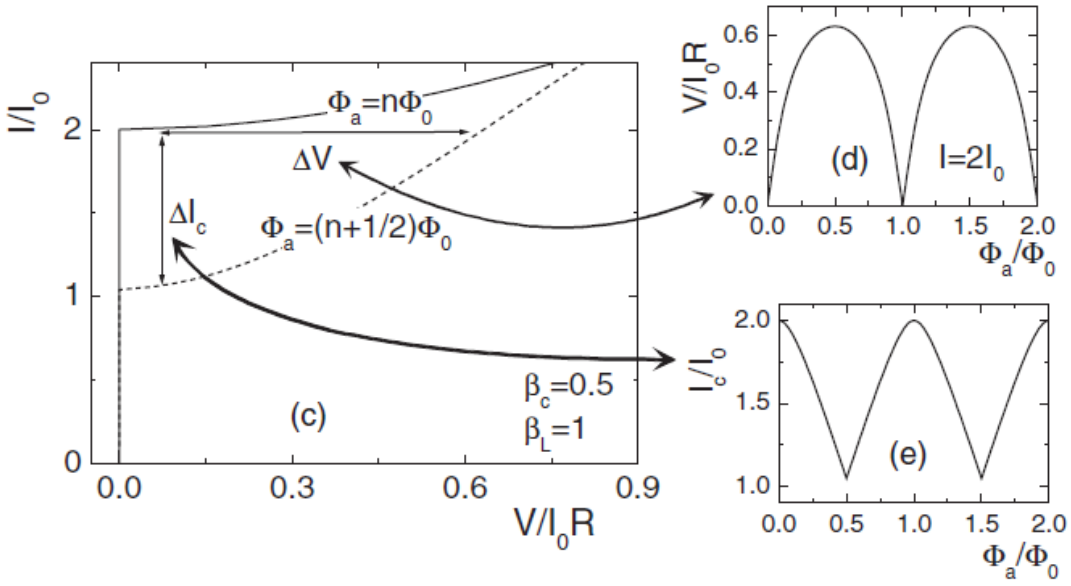

Fig. 3.13 *IV characteristics of DC SQUID with current and voltage variation as a function of flux quantum, adapted by [127].*

reaches a compensating temperature where it shows the minima with further increment due to the moment contribution of the Tm^{3+}.

Zero field Cooling (ZFC): Sample is cooled in the absence of the magnetic field. The warming cycle magnetization as a function of temperature is measured in the presence of the external magnetic field. This method gives the spontaneous magnetization as a function of temperature is experimentally observed.

Field Cooled Cooling(FCC): Sample is cooled in the presence of certainly feeble magnetic field and magnetization as a function of temperature is measured in cooling cycle.

Field Cooled warming (FCW): This process is similar to ZFC, but at the time of cooling, certainly, a small field is applied, and the warming takes place with a magnetic field.

The above three magnetometry modes have been utilized to probe the magnetic transitions in the garnet thin films.

AC Magnetometry

DC magnetometry has limitations in terms of the frequency of the sample oscillations. AC magnetometry can overcome that. In spite of the oscillating sample, a time-dependent AC field is applied with external DC field. This induces the flux in the SQUID to observe the susceptibility (M/H) of the sample. This mode is not absolute, but based on the measurement of the slope of the magnetization vs magnetic field. The advantage of this method is that a small change in slope, no matter how high the moment is, can give the signature of the transitions. The difference between spin ice and superparamagnetic behavior can be understood by taking the AC-susceptibility at various applied AC-magnetic fields. Different sections of the M(H) can be probed by varying the applied DC magnetic field, and the transition and magnetic behaviors can be studied.

3.3.7 Ferromagnetic Resonance

Matter and radiation interact when the condition satisfies between the energy levels of the matter and the energy or frequency of the interacting radiation. This interaction happens and causes the emission or absorption of electromagnetic radiation. Interactions between matter and radiation are the basis of many biological (vision of eyes, sensation of heat with nervous system of the body) and telecommunication devices (radios, television, internet). Matter-radiation interaction helps to understand various fundamentals of matter and science experimentally. The study of this interaction as a function of wavelength or frequency of radiation is termed spectroscopy. Specific absorption or emission frequency of the radiation determines the energy extent of the interaction and gives details of matter; infrared radiation gives details of rotational and vibrational energy levels of interacting materials, and microwave causes molecular rotation and gives details of the electronic levels. By exposing the matter to radiation, its characteristics can be determined by absorption or emission. When the spontaneously magnetized materials (ferromagnetic

and ferrimagnetic) interact with the microwave, their Larmor precession resonant with the specific frequency of the exposed frequency and shows the absorption of that specific frequency. This phenomenon is termed FMR, which can be utilized to calculate various material-specific properties like the gyromagnetic ratio (γ), Gilbert damping parameter (α), anisotropy field (H_K) and saturation magnetization (M_S). FMR is a spectroscopy technique that probes the precession of magnetic components and helps study the dissipative energy factor and the characteristics of magnetically ordered systems. With an external microwave excitation, the precession of magnetization can be probed. FMR was discovered by Griffith in 1946 [46], and the first explanation of the FMR was done by Kittel in 1948 [128]. Historically, the source of microwave radiation was klystrons, and the microwave traveled through the microwave waveguide to the samples placed in the microwave cavity [129]. The resonance cavity works at a certain frequency, which became its limitation along with the high Q-factor. This was overcome using the stripline transmission lines, which had the advantage that various frequencies could be guided and the area of the sample exposed to the microwave was precise [51]. There are two types of stripline, i.e., microstrip and co-planar waveguide [51]. New ways through which the FMR has the potential to be used in cryogenic temperatures and quantum systems, i.e., the varying the gap between the stripline and performing the FMR at variable frequencies and extracting the spin wave dispersion [130].

Working Principle and Instrumentation

The effective magnetic field contributes to splitting energy levels in the magnetically ordered materials. According to Planck's equation, the energy difference (ΔE) of the non-degenerated levels is expressed in terms of a certain frequency. ΔE is proportional to the $g\mu_B B_{eff}$, where g, μ_B and B g-factor, Bohrs magneton and magnetic flux density, respectively. If this system is exposed to external radiation of equivalent frequency, it is

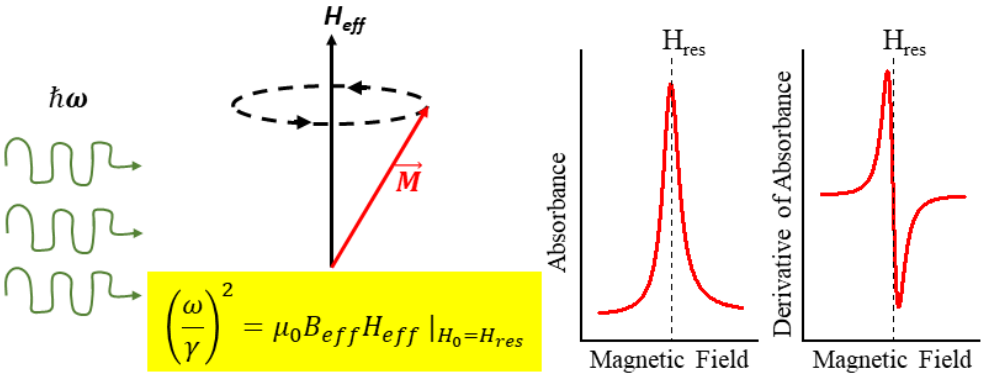

Fig. 3.14 *Microwave radiation of energy ħω falls on the precession magnetization (**M**) along the effective field (H_{eff}) resonate at resonance magnetic field (H_{res}) shows absorbance in the spectra. The first derivative of absorbance is observed in FMR spectra.*

microwaved, which produces resonance. In other words, as the LLG equation give the precession of the magnetization (**M**) along the effective magnetic field (H_{eff}), and it has a frequency of precession and if the system is exposed to equivalent frequency radiation and it shows resonance and that shows absorption in the spectrum as depicted in Figure (3.14) [47, 131].

The instrument of the FMR consists of a microwave source, electromagnet, AC source for the Helmholtz coils for the modulation frequency of the lock-in amplifier, and cavity or the waveguide as presented in Figure (3.15). The waveguides are used for variable frequencies [51]. Broadly, stripline and co-planar waveguides are used. In this work, a co-planar waveguide has been used. In an external magnetic field, the sample's magnetization is excited using the microwave radiation from the co-planar waveguide. A co-planar waveguide is present in between electromagnet and Helmholtz coils where electromagnet provides DC magnetic field and Helmholtz coil provides AC magnetic field. RF source acts as input RF wave, and as RF frequency passes through the co-planar waveguide on which the inverted sample absorbs some band of frequency at resonance magnetic field. RF diode

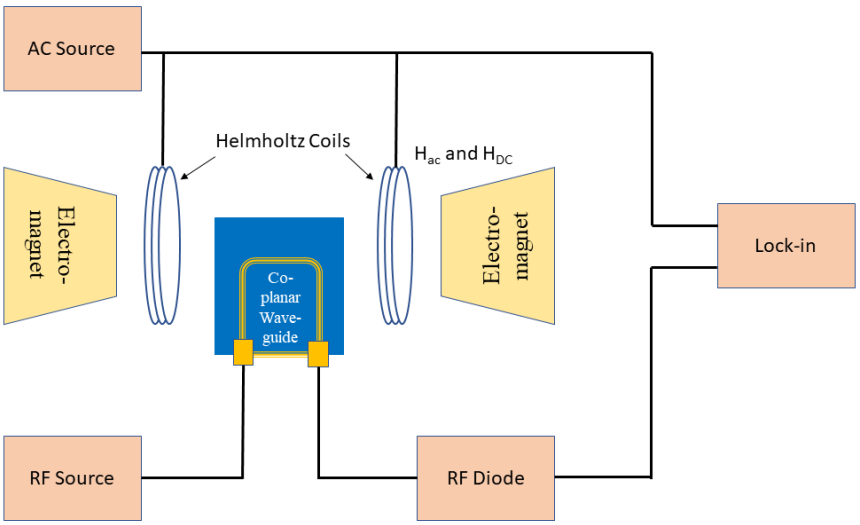

Fig. 3.15 *Ferromagnetic resonance experimental setup.*

measures the absorbed frequency, and the lock-in amplifier enhances the signal-to-noise ratio using a magnetic field. For room temperature FMR with the microwave frequency range 2-10 GHz of Quantum design NanOsc phase FMR has been utilized in this work [132].